JOURNAL OF SPACECRAFT AND ROCKETS
Vol. 44, No. 1, January–February 2007

Calculation of Stagnation-Point Heating Rates Associated with Stardust Vehicle

Chul Park*
ELORET Corporation, Sunnyvale, California 94087

DOI: 10.2514/1.15745

Stagnation-point heating rate is calculated for the Stardust entry vehicle and for its heat-shield models tested in an arcjet wind tunnel. The calculations are made for the convective component for both the laminar and turbulent cases, the radiative component produced by the gas flow, and the radiative component produced by solid particles. A one-dimensional viscous shock layer method is used with an up-to-date thermochemical, gas–surface interaction, radiation, turbulence, and particulate models. For the flight cases, radiation absorption in the boundary layer is found to increase the convective heating rate by a factor of up to two. The calculated sums of all heating rates for the flight cases are nearly the same as those obtained by Olynick et al., and are substantially larger than those by Gupta. The calculated sums of all heating rates for the arcjet test cases are smaller than those calculated by the formula of Fay and Riddell, and are nearly the same as those experimentally determined using copper calorimeters.

Nomenclature

d	=	mixing length, Eq. (8)
h	=	normalized turbulence energy, Eq. (11)
k	=	Boltzmann constant, 1.3806×10^{-23} J/K
k_w	=	surface catalytic velocity, m/s
m	=	mass of one gas molecule, kg
$\dot{m}$	=	ablation rate, kg/(m$^2 \cdot$ s)
p	=	pressure, atm
q_c	=	convective heat flux at wall in the presence of radiation, W/cm^2
q_{c0}	=	convective heat flux at wall in the absence of radiation, W/cm^2
q_p	=	radiative heat flux at wall due to particles, W/cm^2
q_r	=	radiative heat flux at wall due to gas radiation, W/cm^2
R	=	nose radius, m
Sc	=	Schmidt number
T_w	=	wall temperature, K
u_∞	=	freestream velocity, cm/s
v_w	=	injection velocity of ablation product, m/s
ϵ	=	eddy viscosity, m^2/s
η_c	=	probability of gas–surface reaction, Eq. (1)
η_r	=	probability of surface catalytic recombination, Eq. (2)
η_s	=	probability of sublimation, Eq. (3)
μ	=	viscosity, m^2/s
ρ_∞	=	freestream density, kg/m^3
τ	=	characteristic time constant for injection-induced turbulence, Eq. (8), s

Subscripts

e	=	edge of boundary layer
s	=	stagnation point
∞	=	freestream

Presented as Paper 0190 at the 43rd Aerospace Sciences Meeting, Reno, NV, 10–13 January 2005; received 25 September 2005; revision received 3 September 2006; accepted for publication 10 September 2006.

*Senior Research Scientist; currently Department of Aerospace Engineering, Korea Advanced Institute of Science and Technology, 373-1 Guseong-dong, Yuseong-gu, Daejeon, Korea 305-701; cpark216@kaist.ac.kr. Fellow AIAA.

Introduction

THE heating rates over the heat shield for the Stardust entry vehicle during its Earth entry flight have been calculated, among others, by Olynick et al. [1] and Gupta [2]. The calculation by Olynick et al. was made accounting for thermochemical nonequilibrium, whereas the calculation by Gupta assumed equilibrium. Both calculations used the best set of transport properties and radiation database available at the time of the calculation. The flowfield was assumed to be laminar and thermochemical equilibrium was assumed between the gas and the surface at the ablating wall. The possible presence of solid particles in the flow during ablation was not considered.

Since these two works, advancement was made in several areas: a comprehensive set of transport properties and the parameters needed for implementation of the kinetic boundary conditions for the ablating environment (which is believed to be more accurate than the assumption of gas–surface equilibrium) were generated in [3]. A database for the calculation of radiative transport more accurate than that used by Olynick et al. [1] was generated in [4]. The turbulence produced by ablation is characterized in [5]. The radiation by the spalled particles is characterized in [6].

The first purpose of the present work is to redo the earlier calculations for the Stardust flight conditions using these up-to-date techniques.

A series of tests was performed in the years 2001 and 2002 in the Interaction Heating Facility of NASA Ames Research Center to test the ablation behavior of the heat-shield material used for the Stardust vehicle [7]. Tests were made at four different test conditions. The stagnation-point heating rate was measured using a copper calorimeter. For two of these test conditions, a spectral emission measurement and laser beam attenuation measurement were made simultaneously.

The question arises as to how similar were the heating rates at the surface of the ablating models to those measured by the calorimeter and those expected in flight. Because an ablating wall has surface chemical properties different from those of a copper calorimeter, the heat fluxes are expected in general to be different between the two surfaces even when the freestream conditions are the same. The second purpose of the present work is to answer such questions, and thereby provide a database to be used in the interpretation of the results of the arcjet experiment.

For one of the two conditions for which spectral and laser attenuation measurements were made, the spectrum expected in the

test was calculated and compared with the experimental data. A reasonable agreement was found between the calculation and the experimental data.

The heat transfer rates for the Stardust vehicle calculated in the present work are found to be roughly the same as those obtained earlier by Olynick et al. [1] and substantially larger than those by Gupta [2]. The heat transfer rates to the ablating wall in the arcjet test were nearly the same as those to the copper calorimeters. The arcjet test covered the range of values expected for the Stardust vehicle with an appreciable margin.

Method of Calculation

Flowfield

Viscous Shock Layer Method

The flowfield was calculated using a viscous shock layer code for a nonequilibrium flow, which was developed originally in [8] and has been improved over the years. The code is for the stagnation point only, but accommodates two-temperature nonequilibrium chemistry and radiative cooling and absorption. The postshock conditions, which constitute the outer boundary conditions, are determined through the use of the Rankine–Hugoniot conditions of a frozen flow. The code correctly reproduces Fay and Riddell values in the high Reynolds number regime. Unlike the computational fluid dynamic (CFD) method, which encounters a singularity along the stagnation streamline, the viscous shock layer equations written for the stagnation streamline are free of singularities. Therefore, for the purpose of obtaining the solutions along the stagnation streamline, the viscous shock layer method is preferred over the CFD method.

The code was used to calculate the heating environment for Apollo 4 in [4]. Therein, a 20-species, two-temperature nonequilibrium gas model and a transport properties model compatible with it was used. The bifurcation model given in [3] was used in expressing species diffusion in both species conservation and energy conservation equations. The same code with the same input parameter package was used in the present work.

The Stardust vehicle has a spherical nose of 23 cm radius. For the arcjet wind tunnel test, the test models were in the shape of a flat disk with rounded corners. The flowfield around the stagnation point of the flat disk was approximated by that around a sphere of an equivalent nose radius to be explained later.

Gas–Surface Interaction

The heat-shield material of the Stardust entry vehicle is a phenolic impregnated carbon ablator (PICA). The arcjet tests were made using the same material [7]. The general principle of how to specify the species concentrations at the ablating surface is described in detail in [9]. For the carbonaceous ablating surface, there are three kinds of surface reactions: gas–solid reaction of the form

$$\mathrm{X} + \mathrm{C(s)} \rightarrow \mathrm{CX} \tag{1}$$

surface catalytic recombination of the form

$$\mathrm{X} + \mathrm{X} \rightarrow \mathrm{X_2} \tag{2}$$

and sublimation of the form

$$\mathrm{C}_n\mathrm{(s)} \rightarrow \mathrm{C}_n \tag{3}$$

The probability of these thee reactions will be designated here η_c, η_r, and η_s, respectively. The surface recombination probability η_r is related to the so-called catalytic velocity k_w by

$$k_w = \frac{\eta_r}{4}\sqrt{\frac{8kT_w}{\pi m}}$$

where m is the mass of the atom under consideration.

The probability of the surface reaction

$$\mathrm{O} + \mathrm{C(s)} \rightarrow \mathrm{CO} + 3.74\ \mathrm{ev} \tag{4}$$

for a smooth wall is known to be expressible as $\eta_c = 0.63\exp(-1160/T_w)$ [10]. At the wall temperatures encountered in the present work, the η_c attains a value typically of 0.4. The ablating wall is always rough. Surface roughness drives the probability value toward unity [10]. As mentioned in [4], surface catalytic recombination

$$\mathrm{O} + \mathrm{O} \rightarrow \mathrm{O_2} + 5.08\ \mathrm{ev} \tag{5}$$

has been experimentally observed not to occur to any measurable extent, and therefore $\eta_r = 0$ for the reaction.

The probability of the surface reaction

$$\mathrm{N} + \mathrm{C(s)} \rightarrow \mathrm{CN} + 0.35\ \mathrm{ev} \tag{6}$$

has been determined experimentally in [11] to be about 0.3. Surface roughness will drive this probability toward unity also. The surface catalytic recombination

$$\mathrm{N} + \mathrm{N} \rightarrow \mathrm{N_2} + 9.8\ \mathrm{ev}$$

has never been seen experimentally.

The sum of the probabilities for the two processes, Eqs. (1) and (2), for one species must be equal to or less than unity by the definition of a probability. Because the two surface reactions, Eqs. (4) and (6), have a large probability, and because an ablating surface is rough, it is prudent to assume $\eta_c = 1$ for both of these surface reactions. This forces η_r to be zero for both O and N. Most of present calculations are made using this set of η_c and η_r. However, for the purpose of comparison, $\eta_c = \eta_r = 0.5$ is considered also. As will be shown later, the heat transfer rates differ little between these two sets of η values.

At the conditions expected both in flight and in arcjet tests, sublimation of carbon will produce mostly $\mathrm{C_3}$. The rate of sublimation is characterized in general by the sublimation coefficient and equilibrium vapor pressure. The sublimation coefficient is taken from [12] to be

$$\eta = 30\exp(-21,490/T_w)$$

In [3], the equilibrium vapor pressure was deduced from the experiment in [12] made over a relatively small temperature range between about 2000 and 2500 K. The activation temperature in that expression was 59,410 K. In the present work, the surface temperature will be 3000 K or higher. For this temperature range, the expression used in [3] is not appropriate. Instead, the theoretical vapor pressure value given in [13] is used in the present work, according to which the activation temperature is 94,240 K.

Mass Injection Rates

The mass injection rate at wall, i.e., ablation rate, is taken from [1] to be 0.031, 0.064, 0.089, 0.082, 0.056, and 0.037 $\mathrm{kg/(m^2 \cdot s)}$ at the flight times of 42, 48, 54, 60, 66, and 76 s, respectively. These ablation rate values in [1] had been determined by integrating the materials response equations. Olynick et al. [1] do not provide the values of pyrolysis-gas injection rate. Pyrolysis-gas injection rates were determined in the present work by subtracting the surface mass loss rates due to the surface reactions (3), (4), and (6) from the ablation rates. The elemental mass fractions in the pyrolysis gas are considered to be 37.5% C, 46.3% O, and 16.2% H, which are the values accepted in the community.

Gas Radiation

Park [4] points out that a significant development has occurred in the modeling of radiative heating phenomenon recently. In the superorbital Earth entries such as that of the Stardust vehicle, radiative heating originates mostly from oxygen and nitrogen atoms. The radiation by these two atomic species have been characterized until recently by the atomic lines totaling about 300. All previous radiation calculations, including those by Olynick et al. [1] and Gupta [2], were made accounting for this number of lines. Very recently, National Institute for Standards and Technology (NIST) expanded the atomic line data set to include about 1700 lines of oxygen and nitrogen [14]. Atomic line radiation from all these lines was calculated accounting for thermochemical nonequilibrium through the quasi-steady state procedure using the computer code NEQAIR96 [15]. The Stark broadening due to electrons for the newly added atomic lines is calculated by the default formula given in the NEQAIR96 code. For the molecular radiation by N_2 and N_2^+, for which nonequilibrium radiation parameters are known, the nonequilibrium radiation calculation was performed. For CO and CN, for which nonequilibrium radiation parameters are unknown, Boltzmann distribution was assumed.

When these newly added atomic lines are included in the calculation, but not the possibly neglected molecular band systems, the radiation intensity values calculated for the Apollo 4 vehicle were significantly greater than the values measured in flight [4]. In [4], the database for the molecular radiation was expanded for N_2, CO, and H_2, mostly in the vacuum ultraviolet wavelength region. By accounting for these newly added molecular systems simultaneously with the added atomic lines, the flight data for the Apollo 4 vehicle were satisfactorily reproduced.

In the present calculation, the radiation database used for the Apollo 4 calculation in [4] was used. A few calculation details, such as the choice of wavelength ranges, number of wavelength points, the extent to which the line wings are calculated, etc., are the same as those used in [4].

The interaction between gas flow and radiation is calculated iteratively. The flowfield in the absence of radiation is calculated first. Radiative transfer is calculated from the calculated nonradiating flowfield, and the radiative power absorbed by the gas medium is then calculated at each point in the flowfield. The flowfield is solved again including the effect of the radiation absorption.

Park [4] points out that, in the presence of radiation, the convective heating rate at the ablating wall is increased substantially by the absorption of radiation in the boundary layer. For the purpose of elucidating this point, the convective heating rate in the absence of radiation, q_{c0}, will be shown as well as that in the presence of radiation, q_c, obtained through the iteration.

Turbulence

Park [5] pointed out that, according to the measurements made before 1980 at several laboratories at high ablation rates, the ablation rate at the stagnation point of a blunt body made of carbonaceous heat-shield material is higher than calculated assuming the boundary layer flow to be laminar, even when the wall temperature is not high enough to produce significant sublimation. It is known that the roughness of the surface cannot produce turbulence at the stagnation point [5]. But there are evidences of turbulence when the injection is made through a porous cold wall [5]. From these, it was reasoned in [5] that the mass injection by ablation is the cause of the turbulence. The flow is believed to be turbulent at the wall and decays in the boundary layer due to viscous dissipation.

By assuming an appropriate value of wall turbulence intensity, and carrying out the turbulence decay calculation given in [16], the measured ablation rates were numerically reproduced in [5]. The turbulence intensity at the wall that reproduces the measured ablation rate was deduced from the calculation. The theoretical model is termed in [5] the injection-induced turbulence model. According to this model, the turbulence viscosity at the ablating wall is expressible as

$$\epsilon_w = 0.4\dot{m}d \tag{7}$$

The quantity d is given by

$$d = d_m\left[1 - \exp\left(-\frac{\tau v_w}{d_m}\right)\right] \tag{8}$$

where d_m is

$$d_m = 35\sqrt{\frac{\rho_e\mu_e}{2(du_e/ds)}} \tag{9}$$

The quantity du_e/ds is the tangential velocity gradient

$$\frac{du_e}{ds} = \frac{1}{R}\sqrt{\frac{2(p_e - p_\infty)}{\rho_e}} \tag{10}$$

The normalized eddy viscosity h

$$h = \left(\frac{\rho_w}{\epsilon_w}\frac{\epsilon}{\rho}\right)^2 \tag{11}$$

satisfies an ordinary differential equation

$$\left(\frac{1}{Sc}\frac{\rho(\mu+\epsilon)}{\rho_e\mu_e}h'\right)' + fh' - Gh^{3/2} = 0 \tag{12}$$

Here, f is the well-known stream function in the boundary layer coordinate, and G is a quantity

$$G = 0.21\frac{\sqrt{e_w}}{(du_e/ds)d} \tag{13}$$

The primes in Eq. (12) denote differentiation with respect to the transformed coorindate. The differential equation, Eq. (12), must be integrated numerically. The boundary condition for Eq. (12) is that, at the wall, $h = 1$, and at the boundary layer edge, $h = 0$. From the solution h, the eddy viscosity ϵ is calculated and added to the intrinsic viscosity μ to obtain the effective viscosity.

The parameter characterizing the phenomenon is the quantity τ in Eq. (8), which has the units of seconds: a larger value of τ signifies stronger turbulence. For graphite and carbon–carbon, τ is found in [5] to be about 2×10^{-4} s. Park and Balakrishnan [17] find that this value is acceptable for carbon–phenolic also. In contrast, sintered beryllium or stainless steel is found to have a τ value two orders of magnitude greater. The injection-induced turbulence method was used in numerically reproducing the thermocouple data obtained during the entry flights of the four Pioneer-Venus vehicles with a modest success [18,19].

For the PICA material considered in the present work, there are no data for τ. It is assumed to be 2×10^{-4} s, the value for graphite, carbon–carbon, and carbon–phenolic, in most of the present work. A value of 4×10^{-4} was used for one case for comparison, to show that the calculated heat transfer rate is relatively insensitive to τ.

Solid Particle Radiation

In [6], the radiation of solid particles injected into the flow from the ablating wall is characterized. The work is based on a laser beam attenuation measurement made in the aforementioned arcjet test [20]. A He–Ne laser beam was found to be attenuated in passing through the shock layer over an ablating PICA model. This was interpreted to be due to the blockage by small particles ejected from the ablating wall. The trajectory of a solid particle ejected from the ablating wall is calculated accounting for the heating by the colliding gas atoms and molecules and the surface chemical reactions, Eqs. (4) and (6), and cooling by surface radiation and sublimation. By knowing the radius of the particle as a function of spatial position, one can calculate the blockage of the laser beam by that particle at that position. The initial

diameter of the particle and its ejection velocity are assumed to obey a simple distribution law. The parameters governing the particle size and ejection velocity are varied until the aggregate blockage of the laser beam agreed with the experimental data. There are five unknown parameters, two each for size and velocity, and one for the absolute quantity of solid particles. Park et al. [6] found that the experiment rendered four parameters, leaving one, the median size, arbitrary. The median size was deduced to be less than 20 μm from the fact that there is no bend in the attenuation pattern across the shock wave.

Park et al. [6] show that, for all possible particle sizes below 20 μm, the absolute quantity of the solid particles is too small to affect the flowfield. However, the surface radiation by the particles is substantial. The surface radiation by the particles is unaffected by the choice of the median size, as long as the five parameters are selected to reproduce the experimental data.

The four conditions tested in [20] covered the entire range of possibilities of particle radiation for the Stardust entry conditions. By means of a logarithmic interpolation, the particle effect for the Stardust flight case was calculated for the flight conditions. Thus, Park et al. [6] give the heat flux values at the stagnation point q_p of the Stardust vehicle due to the particle radiation. These values are adopted in the present work.

Arcjet Test

Testing Environment

The arcjet experiment was made in the Interaction Heating Facility of Ames Research Center. All tests were made at one operating condition of the arc heater. The test gas was dry air, i.e., the natural air with water vapor removed, plus about 7% by mass of argon. This concentration of argon is the main difference between the arcjet test and flight. The test gas is believed to have contained carbon dioxide to a mol concentration of the order of 0.1%, and, as is usually the case, an unknown concentration of hydrocarbon species originating from vacuum pumps. Presence of hydrocarbon in the stream is immaterial in the present test because the ablator produces pyrolysis gas, which is a mixture of many hydrocarbon species. The pressure in the plenum chamber was 4.5 atm at this operating condition. The enthalpy was determined by four different methods [21]. The heat balance and sonic throat method both resulted in an average enthalpy value of about 29 MJ/kg. The heat transfer rate to a copper calorimeter at the stagnation point of a flat circular disk gave a minimum enthalpy value of 30 MJ/kg. By analyzing the spectrum of the radiation emitted by the shock layer, enthalpy value was determined to be 40.6 ± 1.4 MJ/kg [21].

Two different nozzles were used: one with an exit diameter of 15.2 cm and the other with a 30.5 cm exit diameter. Based on the pitot impact pressure measurement, the effective area ratios at the location of the tested models for these two nozzles were judged to be 10 and 42, respectively. The tested models were in the shape of a circular flat disk with rounded corners. The corner radius was 18.75% of the base radius of the model. The base diameter of the model was varied as 2.54, 4.08, and 10.2 cm. The tests were made at four different combinations of model sizes and nozzle area ratios. The operating conditions were identified in [21] as conditions 1 through 4. The heating rates were measured at the stagnation point of the models made of copper through calorimetry as mentioned. The measured values were 1100 W/cm^2 for condition 3 and 1630 W/cm^2 for condition 4 [6]. Table 1 summarizes the operating conditions for the four conditions and the measured heating rate values to the copper calorimeters.

The flow over a flat disk with a rounded corner produces a shock standoff distance and boundary layer thickness that are different from those for a sphere but are equal to those of a sphere with a certain radius. The relationship between this equivalent sphere nose radius and the geometry of the flat disk is well known and is used in [21]. Using this relationship, the flat disk is represented in the present work by a sphere of that radius.

The measured recession rates varied slightly with time. For instance, for condition 4, the recession rate varied from about 0.75 mm/s to about 0.88 mm/s depending on the time after the commencement of ablation. The peak value is used in the present work in calculating the heating rate and the turbulence behavior. By assuming that the char depth advances at the same rate as the surface recession, i.e., a steady ablation, one obtains the mass injection rate by multiplying the recession rate by the density of the PICA material, 240 kg/m^3. The char was found to have a density 40% less than the virgin material. By assuming that the char depth advanced at twice the surface recession rate, the mass injection rate is determined to be 1.4 times the steady ablation value. Both these mass injection values are used in the present work.

Table 1 Summary of four conditions in the arcjet test; see [21]

Condition No.	1	2	3	4
Nozzle exit diameter, cm	30.5	30.5	15.3	15.3
Effective nozzle area ratio	42	42	10	10
Pitot impact pressure, atm	0.16	0.16	0.66	0.66
Model base diameter, cm	10.2	10.2	5.08	2.54
Equiv. sphere nose radius, cm	16.0	16.0	8.0	4.0
Fay–Riddell q_c, W/cm^2	566	1050	1450	2100
Copper calorimeter q_c, W/cm^2	400	580	1150	1630
Nominal recession rate, mm/s	0.11	0.22	0.44	0.88
Particle radiation q_p [5], W/cm^2	8.3	54.5	72.9	168

Surface Catalysis for Copper Calorimeters

The catalytic efficiency η_c for pure copper is believed to be about 0.4 [22]. But, in an environment with high concentration of atomic oxygen and an elevated wall temperature, the copper surface easily becomes oxidized [23]. The η_c for copper oxide is estimated in [22] to be about 0.02. In the present work, calculations are made for the η_r values of 0.01, 0.02, and 0.4.

Spectrum

As mentioned, emission spectrum was obtained for two conditions, conditions 3 and 4, during ablation [21]. No absolute intensity calibration was made. Simultaneously with the spectral measurement, the extent of attenuation of a laser beam across the shock layer was measured [21]. For condition 3, the spectral measurement and the laser attenuation measurement are coordinated so that the results of one measurement can be used for the interpretation of the other [20].

Specifically, at the point immediately ahead of the bow shock wave, the measured laser attenuation yielded the attenuation to be about 4%. The spectral emission from this region was found to be that of a black body at a temperature of about 3700 K. Within about 3 mm in the axial direction, the attenuation value fell to zero. The spectral data obtained for this preshock region are, by the averaging process in the measuring instrument, a spatial average over about 3 mm. Therefore, the spectral data in the preshock region represent an emission from the cloud of particles radiating as a black body at 3700 K covering 2% of the viewing field.

By so recognizing the emission in this preshock region, one can use this information as an absolute intensity calibration for the shock layer radiation for that particular run. This was done for the condition 3 data. The absolute spectrum so derived is then compared with the calculated absolute spectrum. To calculate the absolute spectrum emitted by the shock layer, the radiating field was assumed to be one-dimensional, i.e., uniform in the radial direction over the entire diameter of the model. That is, the thermodynamic state is assumed to be uniform and to have the property along the stagnation streamline. Radiative transport calculation is made for this field.

The radiation calculation obviously tends to overestimate the radiation intensity because the flow is cooler at points away from the stagnation streamline. Nevertheless, the procedure provides a means of verifying the general accuracy of the procedure, perhaps to within a factor of 2.

Results

Stardust Flight Cases

General Features of Solutions

The pyrolysis-gas injection rates for the Stardust vehicle calculated in the present work are compared with the given ablation rates, i.e., sum of the pyrolysis-gas injection rate and wall removal rate, in Fig. 1. As seen here, pyrolysis-gas injection rate is a significant or a dominant fraction of the ablation rate; its contribution reaches 78% at the peak-heating trajectory point of 54 s. Relative contribution of pyrolysis gas becomes small toward the end of the heating period as expected.

The strength of turbulence produced by mass injection at wall is shown in Fig. 2 in the form of the ratio $\rho(\mu+\epsilon)/(\rho\mu)_{\text{shock}}$ for the trajectory point of 54 s. The figure compares this ratio to the same ratio for a laminar flow, $\epsilon = 0$. As mentioned earlier, the turbulent eddy viscosity ϵ is produced at the stagnation point solely by the mass injection at the wall, and is proportional roughly to the mass injection rate. As seen here, ϵ is a relatively small fraction of $\mu+\epsilon$. This foreshadows that the effect of injection-induced turbulence will be relatively small for the Stardust vehicle.

In Fig. 3, temperature distribution in the boundary layer is shown for the trajectory point of 54 s for the laminar case without radiation, laminar case with radiation, and turbulent case with radiation. As seen in the figure, radiation affects temperature distribution significantly: temperature is lowered in the outer region of the boundary layer and raised near the wall. The effect of turbulence is relatively minor. Though not shown, shock standoff distance is not changed much by radiation: 15.3 mm without radiation and 16.7 mm with radiation. (These values are considerably larger than the 13 mm value obtained by Olynick et al. [1]. The difference arises from the shock-fitting method used in the viscous shock layer solution as opposed to the shock-capturing method in CFD. The postshock temperature in the present solution is 58,680 K as opposed to 24,000 K by Olynick et al.) In any case, the rise in temperature near the wall causes the temperature gradient at wall to rise.

In Fig. 4, radiative heat flux and convective heat flux are shown for the 54 s trajectory point. Convective heat flux is a sum of the conductive heat flux (conductivity times temperature gradient) and chemical energy fluxes (diffusion coefficient times species concentration gradient times chemical energy). This convective heat flux does not necessarily approach the wall convective heat flux value because not all of the chemical energy is converted to heat at wall: the extent of conversion of chemical energy to heat at wall is determined by the surface reaction rates. However, this quantity is a useful indicator of convective energy transport.

For the no-radiation case, convective heat flux behaves in a way typical to all boundary layer phenomena: a nearly monotonic increase from zero at the boundary layer edge to a finite value at wall. However, when radiation exists, convective flux increases sharply near the wall. The increase in convective heat flux corresponds to the increase in temperature gradient seen in Fig. 3. The radiative heat flux reaches a peak of 913.4 W/cm^2 at the edge of the boundary layer, and decreases toward the wall, reaching a value of 123.1 W/cm^2 at the wall. Seemingly, the radiative heat flux lost, no doubt by absorption, is partly converted to convective heat flux through a rise in temperature, and 86.5% of radiative heat flux is absorbed in the boundary layer.

The radiative heat flux incident at the boundary layer edge exits from the control volume via two routes: 1) reaching the wall either as radiative or convective heat flux, and 2) convectively discharged

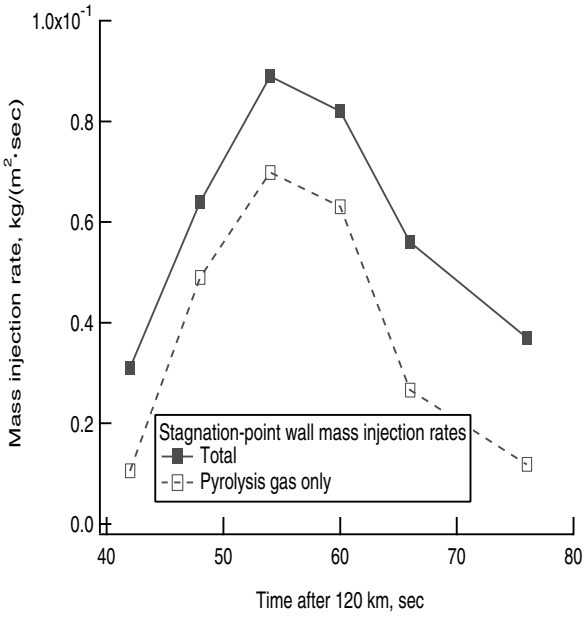

Fig. 1 Mass injection rates at wall.

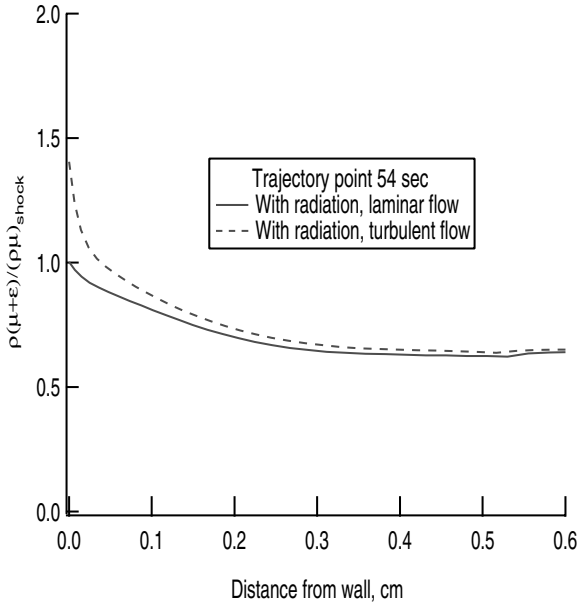

Fig. 2 The ratio $\rho(\mu+\epsilon)/(\rho\mu)_{\text{shock}}$ for the turbulent flow case with $\tau = 2 \times 10^{-4}$ s, for the trajectory point of 54 s.

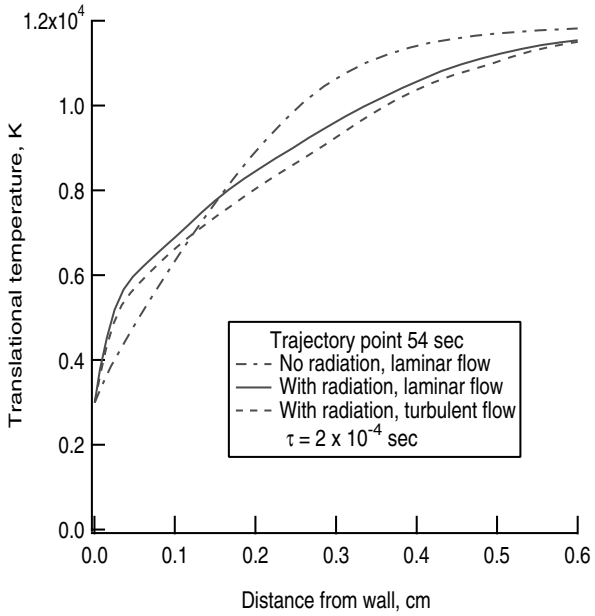

Fig. 3 Distribution of translational temperature within boundary layer at the stagnation point.

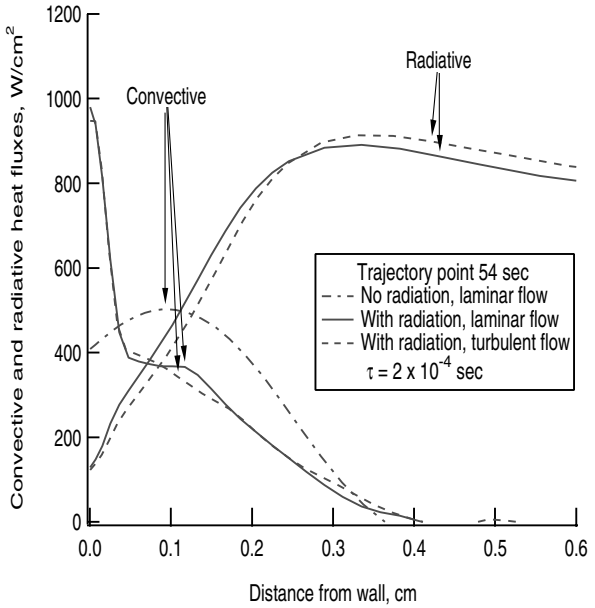

Fig. 4 Radiative and convective heat fluxes in the boundary layer at trajectory point 54 s.

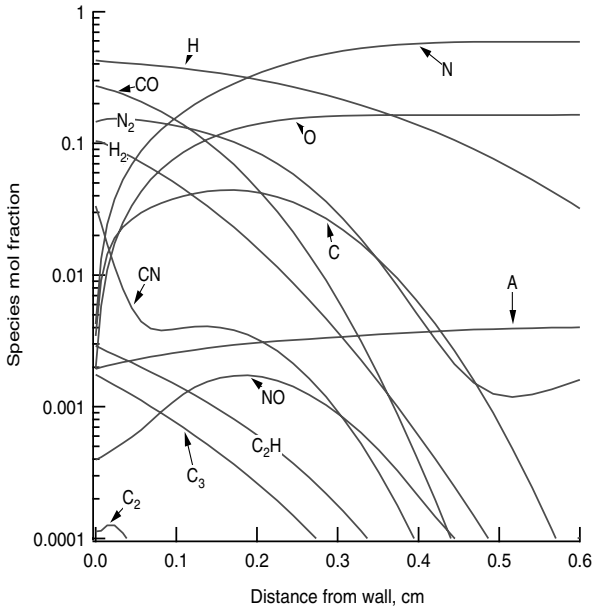

Fig. 5 Distribution of species mol fractions of the major species in the boundary layer for the trajectory point 54 s.

downstream. Of the $913 - 123 = 790$ W/cm^2 absorbed in the boundary layer, 484 W/cm^2 is converted to convective heat flux to raise it from 483 W/cm^2 to 967 W/cm^2 (see Table 2). The rest, $790 - 484 = 306$ W/cm^2, is convectively discharged downstream. This convectively discharged heat flux will appear as an increase in the convective heat transfer rate in the downstream region.

Figure 5 shows the distribution of the major species in the boundary layer for the 54 s case. As seen here, the largest species in the boundary layer are H, H_2, N_2, and CO. H and H_2 originate from the pyrolysis gas injected at the wall. CO originates at the wall as a result of oxidation process, Eq. (4). According to the present model, absorption of radiation by these species occurs mostly in the vacuum ultraviolet wavelength region.

According to the present surface chemistry model, the nitridation process that produces CN, Eq. (6), is expected to be prominent. As Fig. 5 shows, concentration of N is large at the boundary layer edge, and yet concentration of CN is small in the boundary layer. On the other hand, concentration of N_2 is fairly large in the region near the wall, even though it is small at the boundary layer edge and even though catalytic recombination of N is neglected. This phenomenon is due to the gas-phase reaction

$$\mathrm{CN} + \mathrm{N} \rightarrow \mathrm{N_2} + \mathrm{C}$$

which converts CN into N_2. Thus, the fast nitridation produces an effect of high surface catalytic recombination of N.

Heat Transfer Rates

The calculated heat transfer rates are presented in Table 2 and are compared with the values obtained by Olynick et al. [1]. There are three components to the heating rate: convection q_c, gas radiation q_r, and particle radiation q_p. The convective heating rate in the absence

Table 2 Stagnation-point heating rates for the Stardust vehicle; wall temperature is assumed to be 3000 K for all cases

Time after 120 km, sec	42	48	54	60	66	76
Freestream density, kg/m^3	4.16×10^{-5}	1.06×10^{-4}	2.34×10^{-4}	4.39×10^{-4}	7.21×10^{-4}	1.35×10^{-3}
Flight velocity, m/s	12,413	12,004	11,137	9719	7957	5179
Stagnation pressure, atm	0.0553	0.132	0.251	0.358	0.395	0.313
Ablation rate [1], kg/(m$^2 \cdot$ s)	0.031	0.064	0.089	0.082	0.056	0.037
q_c, Fay–Riddell, W/cm^2	482	703	839	746	496	152
q_r, Olynick et al., W/cm^2	8	40	120	48	40	10
$q_c + q_r$, Olynick et al., W/cm^2	720	1000	1220	1040	700	220
			Present calculation, W/cm^2			
q_p (from [5])	8	71	93	59	26	0.2
			Laminar flow			
q_{c0}	253	387	483	463	416	146
q_r	77	146	129	48	32	17
q_c,	697	833	967	721	499	146
$q_c + qr + q_p$	782	1050	1189	828	557	163
			Turbulent flow, $\tau = 2 \times 10^{-4}$ s			
q_{c0}	280	409	505	510	419	148
q_r	74	130	123	49	25	17
q_c	819	885	1045	755	498	153
$q_c + q_r + q_p$	901	1086	1261	863	549	170
			Turbulent flow, $\tau = 4 \times 10^{-4}$ s			
q_{c0}	——	——	540	——	——	——
q_r	——	——	118	——	——	——
q_c	——	——	1061	——	——	——
$q_c + q_r + q_p$	——	——	1272	——	——	——

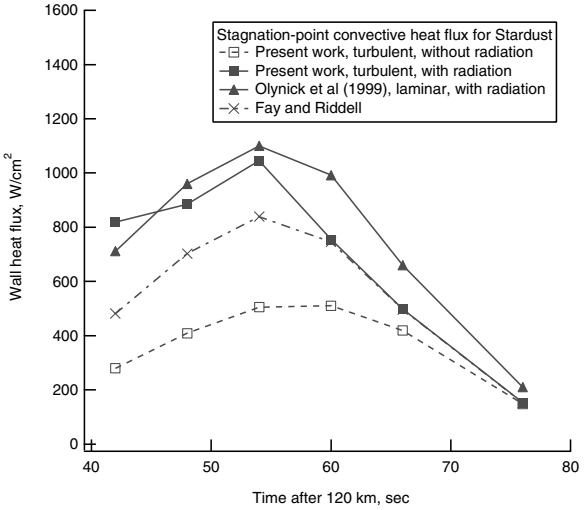

a)

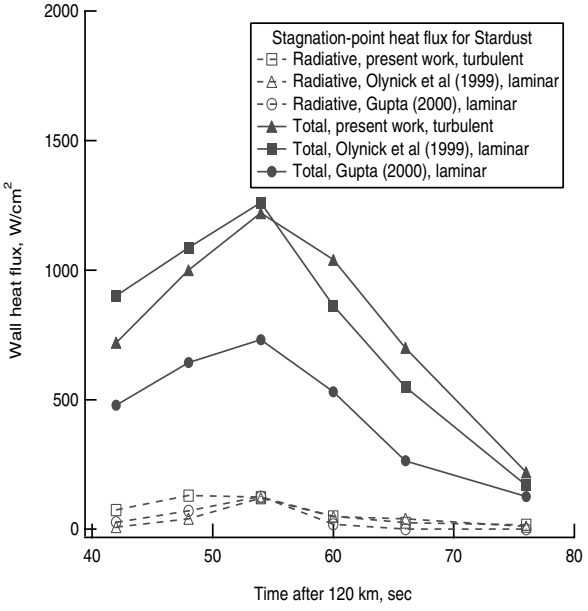

b)

Fig. 6 Comparison between the present results and the earlier results for the Stardust entry vehicle. a) Convective heat fluxes compared with the results of Olynick et al. [1]. b) Radiative and total heat fluxes compared with the results of Olynick et al. [1] and Gupta [2].

of radiation, q_{c0}, is shown for reference. There are three different solutions: laminar, turbulent with $\tau = 2 \times 10^{-4}$, and turbulent with $\tau = 4 \times 10^{-4}$, for both convective and radiative components. Strictly speaking, the particle radiation should also be affected by the laminar/turbulent options. However, in view of the uncertainty in the particle radiation calculation, the q_p values for the laminar case are assumed to be valid also for the turbulent case.

As Table 2 shows, the convective heating rate is increased by radiation to a factor of up to about two. The radiation by particles is up to about 8% of the combination of q_c and q_r. Turbulence increases q_c by less than 10%. The total heat flux values, $q_c + q_r + q_p$, for the turbulent case are roughly the same as those of Olynick et al. [1], even though the latter is for the laminar flow. Doubling the assumed characteristic turbulence parameter τ produces only a very small change in the calculated heating rate.

In Figs. 6a and 6b, the heat flux values obtained in the present work are compared with the values by Olynick et al. [1] and those by Gupta [2]. As seen in Fig. 6a, convective heat flux values of both the present work and the work by Olynick et al., shown both as solid-lined points, are higher than the Fay–Riddell values despite the fact that there is boundary-layer blowing. This is due to the absorption of radiation in the boundary layer. Without radiation, the convective heat flux is indeed lower than the Fay–Riddell value, as shown by the dash-lined points. In both Figs. 6a and 6b, the present calculated values are nearly the same as those by Olynick et al. The radiative heat fluxes reaching the wall are seen to be quite small in both solutions.

As Fig. 6b shows, the equilibrium calculation of Gupta [2] gives total heat flux values substantially smaller than the two other solutions. Because radiative heating rates are small, the difference is in the convective heating rates. The only significant difference between Gupta's solutions and the other two solutions is the magnitude of radiation. For instance, the equilibrium radiative heat flux at the edge of boundary layer for the trajectory point 54 s is determined to be 187 W/cm^2 from the formula given by Tauber and Sutton [24]. Gupta used the method used by Tauber and Sutton to determine the equilibrium radiative flux. As mentioned earlier, the present nonequilibrium calculation gives the radiative heat flux at the boundary layer edge for the same condition to be 913 W/cm^2. Also as mentioned, 484 W/cm^2 of this 913 W/cm^2 is converted into convective heat flux in the present calculation. If 484 W/cm^2 is added to Gupta's value, there will be a fairly good agreement among all three sets of calculations. This points to the need to include nonequilibrium radiation in calculating convective heating rates.

Arcjet Test Cases

Spectrum

The measured and calculated spectra for condition 3 are compared in Fig. 7. As mentioned, the calculation is made assuming that the thermodynamic properties are uniform in the radial direction over the entire diameter of the model. The spectrum ahead of the shock wave agrees approximately with the black body spectrum at 3700 K emitted by 2% of surface area. The spectrum calculated in the shock layer seems to agree with the observed spectrum in the major features, considering the fact that the radiating field was calculated assuming a one-dimensional flow.

Heat Transfer Rates

The calculated heat transfer rates for the arcjet test cases are presented in Table 3. The enthalpy in the tests, 40.6 MJ/kg, is significantly smaller than the enthalpy values during flight, at least for those before the 76 s point. As a result, the radiative heating rate q_r is small for the arcjet cases. The convective heating rates do not increase significantly by the absorption of radiation in the boundary

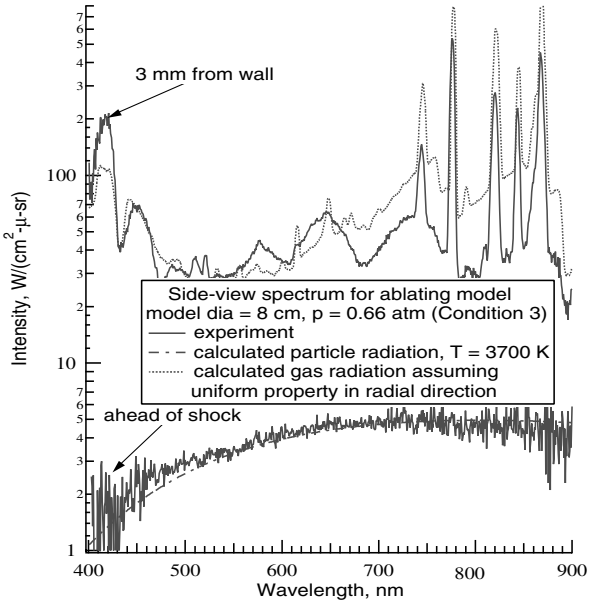

Fig. 7 Comparison of the measured and calculated side-view spectrum.

Table 3 Calculated stagnation-point heat transfer rates to models placed in the Interaction Heating Facility

Condition No.	Model diam., cm	Stagn press., atm	Matl	React prob η_c	Recm prob η_r	Abltn rate kg/(m^2 · s)	T_w, K	q_c Fay–Riddell, W/cm^2	lamin or turb	q_c presnt calc, W/cm^2	q_r presnt calc W/cm^2	$q_c + q_r + q_p$
1	10.2	0.164	Cu	0	0.01	0	700	632	lam	391	0	391
1	10.2	0.164	Cu	0	0.02	0	700	632	lam	488	0	488
1	10.2	0.164	Cu	0	0.40	0	700	632	lam	604	0	604
1	10.2	0.164	PICA	1	0	0.0264	2500	586	lam	446	0	446
1	10.2	0.164	PICA	1	0	0.0370	3000	566	lam	385	0	385
1	10.2	0.164	PICA	1	0	0.0370	2500	586	lam	451	0	451
1	10.2	0.164	PICA	1	0	0.0370	3000	566	lam	418	0	418
1	10.2	0.164	PICA	1	0	0.0370	3000	566	turb	428	10	448
1	10.2	0.164	PICA	0.5	0.5	0.0370	2500	586	lam	456	0	456
1	10.2	0.164	PICA	0.5	0.5	0.0370	3000	566	lam	423	0	423
2	10.2	0.164	Cu	0	0.01	0	700	1140	lam	820	0	820
2	10.2	0.164	Cu	0	0.02	0	700	1140	lam	925	0	925
2	10.2	0.164	Cu	0	0.40	0	700	1140	lam	1020	0	1120
2	10.2	0.164	PICA	1	0	0.0528	2500	1080	lam	782	0	782
2	10.2	0.164	PICA	1	0	0.0528	3000	1050	lam	749	0	749
2	10.2	0.164	PICA	1	0	0.0528	3500	1000	lam	501	0	501
2	10.2	0.164	PICA	1	0	0.0739	2500	1060	lam	733	0	733
2	10.2	0.164	PICA	1	0	0.0739	3000	1030	lam	797	0	797
2	10.2	0.164	PICA	1	0	0.0739	3000	1030	turb	983	13	1051
2	10.2	0.164	PICA	1	0	0.0739	3500	978	lam	384	0	384
2	10.2	0.164	PICA	0.5	0.5	0.0739	2500	1060	lam	736	0	736
2	10.2	0.164	PICA	0.5	0.5	0.0739*	3000	1030	lam	697	0	697
2	10.2	0.164	PICA	0.5	0.5	0.0739	3500	978	lam	384	0	384
3	5.08	0.60	Cu	0	0.01	0	700	1610	lam	1110	0	1110
3	5.08	0.60	Cu	0	0.02	0	700	1610	lam	1290	0	1290
3	5.08	0.60	Cu	0	0.40	0	700	1610	lam	1530	0	1530
3	5.08	0.60	PICA	1	0	0.106	2500	1500	lam	1100	0	1100
3	5.08	0.60	PICA	1	0	0.106	3000	1450	lam	1050	0	1050
3	5.08	0.60	PICA	1	0	0.106	3400	1400	lam	865	0	865
3	5.08	0.60	PICA	1	0	0.148	2500	1500	lam	959	0	959
3	5.08	0.60	PICA	1	0	0.148	3000	1450	lam	915	0	915
3	5.08	0.60	PICA	1	0	0.148	3000	1450	turb	1010	6.8	1090
3	5.08	0.60	PICA	1	0	0.148	3400	1400	lam	801	0	801
3	5.08	0.60	PICA	0.5	0.5	0.148	2500	1500	lam	965	0	965
3	5.08	0.60	PICA	0.5	0.5	0.148	3000	1450	lam	909	0	909
3	5.08	0.60	PICA	0.5	0.5	0.148	3400	1400	lam	810	0	810
4	2.54	0.60	Cu	0	0.01	0	700	2280	lam	1370	0	1370
4	2.54	0.60	Cu	0	0.02	0	700	2280	lam	1710	0	1710
4	2.54	0.60	Cu	0	0.40	0	700	2280	lam	2190	0	2190
4	2.54	0.60	PICA	1	0	0.211	2500	2160	lam	1410	0	1410
4	2.54	0.60	PICA	1	0	0.211	3000	2100	lam	1290	0	1290
4	2.54	0.60	PICA	1	0	0.211	3500	2000	lam	897	0	897
4	2.54	0.60	PICA	1	0	0.296	2500	2160	lam	1140	0	1140
4	2.54	0.60	PICA	1	0	0.296	3000	2100	lam	1110	0	1110
4	2.54	0.60	PICA	1	0	0.296	3000	2100	turb	1500	2.7	1671
4	2.54	0.60	PICA	1	0	0.296	3500	2000	lam	824	0	824
4	2.54	0.60	PICA	0.5	0.5	0.296	2500	2160	lam	1100	0	1100
4	2.54	0.60	PICA	0.5	0.5	0.296	3000	2060	lam	1080	0	1080
4	2.54	0.60	PICA	0.5	0.5	0.296	3500	1960	lam	829	0	829

layer, i.e., q_{c0} and q_c are approximately the same. Therefore, no distinction is made between q_{c0} and q_c in the Table.

Several comments can be made about Table 3. One sees that the heating rates for copper calorimeter vary significantly over the range of uncertainty of the surface catalytic recombination coefficient. Wall temperature has a small but discernible effect in heat transfer rate. The choice of $\eta_c = \eta_r = 0.5$ yields insignificantly larger heating rates. Turbulence increases heat transfer rate by an order of 10% or less.

The highest calculated values of convective heating rates are those with turbulence. In Fig. 8, the total heating rates, $q_c + q_r + q_p$, for the turbulent case are compared with the copper calorimeter values and the peak flight value. For conditions 1 and 2, for which calorimeter measurement was not made, the inferred values given in Table 1 are used. The flight value is the total heating rate at the peak-heating point as given in Table 2.

As seen in this figure, the total heating rates to the ablating models are fairly close to those of calorimeter. This implies that, by assuming the heating rates to the ablating surface to be those for the copper calorimeter, one would err little. For condition 4, the heating rate applied to the ablating model is appreciably higher than that for the Stardust vehicle at its peak-heating point. This means that the tested environment covered the anticipated heating rates with an appreciable margin.

Conclusions

An up-to-date calculation method for calculating the heating rate of an ablating heat-shield made of PICA, accounting for turbulence and particle radiation and incorporating an improved radiation model, yields heating rates at the stagnation point of the Stardust entry vehicle that are nearly the same as those calculated by Olynick et al. [1] and substantially larger than those by Gupta [2]. Radiative heat flux incident on the boundary layer edge is mostly absorbed in the boundary layer. However, over half of the absorbed radiative heat flux is converted to convective heat flux to nearly double the convective heat flux. In the arcjet tests performed, the heating rates to the ablating PICA models were nearly those obtained by the copper

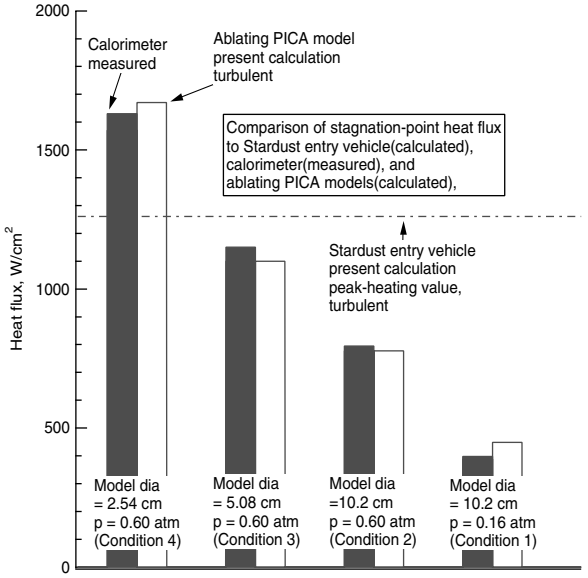

Fig. 8 Comparison of the stagnation-point heating rates among the flight conditions (calculated), the arcjet test conditions with PICA ablator (calculated), and the measured calorimeter values.

calorimeter. The tested environment covered the flight environment with an appreciable margin.

Acknowledgments

The author wishes to acknowledge the support provided by NASA Ames Research Center through the contract NAS2-99092 to ELORET Corporation. The author also wishes to express sincere thanks to G. Raiche, D. Driver, J. Olejniczak, Imelda Terrazas-Salinas, J. Heinemann, and A Covington, all of NASA Ames Research Center, for providing various information used in the present work.

References

[1] Olynick, D., Chen, Y. K., and Tauber, M. E., "Aerothermodynamics of the Stardust Sample Return Capsule," *Journal of Spacecraft and Rockets*, Vol. 36, No. 3, May–June 1999, pp. 442–462.

[2] Gupta, R. N., "Aerothermodynamic Analysis of Stardust Sample Return Capsule with Coupled Radiation and Ablation," *Journal of Spacecraft and Rockets*, Vol. 37, No. 4, July–Aug. 2000, pp. 507–514.

[3] Park, C., Jaffe, R., and Partridge, H., "Chemical-Kinetic Parameters of Hyperbolic Earth Entry," *Journal of Thermophysics and Heat Transfer*, Vol. 15, No. 1, Jan.–March 2001, pp. 76–90.

[4] Park, C., "Stagnation-Point Radiation for Apollo 4," *Journal of Thermophysics and Heat Transfer*, Vol. 18, No. 3, July–Sept. 2004, pp. 349–357.

[5] Park, C., "Injection-Induced Turbulence in Stagnation-Point Boundary Layers," *AIAA Journal*, Vol. 22, No. 2, Feb. 1984, pp. 219–225.

[6] Park, C., Raiche, G. A., II, and Drive, D. M., "Radiation of Spalled Particles in Shock Layers," *Journal of Thermophysics and Heat Transfer*, Vol. 18, No. 4, Oct.–Dec. 2004, pp. 519–526.

[7] Covington, M. A., Heinemann, J. M., Goldstein, H. E., Chen, Y.-K., Terrazas-Salinas, I., Balboni, J. A., Olejniczak, J., and Martinez, E. R., "Performance of a Low Density Ablative Heat Shield Material," AIAA Paper 2004-2273, June–July 2004.

[8] Park, C., "Dissociative Relaxation in Viscous Hypersonic Shock Layers," *AIAA Journal*, Vol. 2, No. 7, July 1964, pp. 1202–1207.

[9] Chen, Y. K., and Milos, F. S., "Finite-Rate Ablation Boundary Conditions for a Carbon-Phenolic Heat-Shield," AIAA Paper 2004-2270, June–July 2004.

[10] Park, C., *Nonequilibrium Hypersonic Aerothermodynamics*, John Wiley, New York, 1990, Sec. 9.5.

[11] Park, C., and Bogdanoff, D. W., "Shock Tube Measurement of Nitridation Coefficient of Solid Carbon," *Journal of Thermophysics and Heat Transfer*, Vol. 20, No. 3, July–Sept. 2006, pp. 487–492.

[12] Baker, R. L., McDonaugh, J. M., Herr, K. C., Klingberg, R. A., Coffer, J. C., and Covington, M. A., "Carbon Vaporization and Condensation Effects," Space Division/AFSC, Report SD-TR-84-53, Los Angeles, CA, July 1984.

[13] Leider, H. R., Krikorian, O. H., and Young, D. A., "Thermodynamic Properties of Carbon up to the Critical Point," *Carbon*, Vol. 11, No. 5, May 1973, pp. 556–563.

[14] NIST Atomic Spectra Database, Ver. 2.0, National Institute of Standards and Technology (NIST) Physics Laboratory, Gaithersburg, MD, http://physics.nist.gov/asd [cited March 1999].

[15] Whiting, E. E., Park, C., Liu, Y., Arnold, J. O., and Paterson, J. A., "NEQAIR96, Nonequilibrium and Equilibrium Radiative Transport and Spectra Program: User's Manual," NASA Reference Publication 1389, Dec. 1996.

[16] Wassel, A. T., and Denny, V. E., "Heat Transfer in Axisymmetric Bodies in Super- and Hypersonic Turbulent Stream," *Journal of Spacecraft and Rockets*, Vol. 14, No. 4, April 1977, pp. 212–218.

[17] Park, C., and Balakrishnan, A., "Ablation of Galileo Probe Heat-Shield Models in a Ballistic Range," *AIAA Journal*, Vol. 23, No. 2, Feb. 1985, pp. 301–308.

[18] Ahn, H. K., Park, C., and Sawada, K., "CFD Calculation of Heat Fluxes in Turbulent Flow for Pioneer-Venus Probes," AIAA Paper 98-0833, Jan. 1998.

[19] Takahashi, M., and Sawada, K., "Simulation of Entry Flight Flowfield over Four Pioneer-Venus Mission," AIAA Paper 2002-0909, Jan. 2002.

[20] Raiche, G. A., II, and Driver, D. M., "Shock Layer Optical Attenuation and Emission Spectroscopy Measurements During Arc Jet Testing with Ablating Models," AIAA Paper 2004-0825, 2004.

[21] Park, C., Raiche, G. A., II, Driver, D. N., Olejniczak, J., Terrazas-Salinas, I., Hightower, T. M., and Sakai, T., "Comparison of Enthalpy Determination Methods for an Arc-jet Facility," *Journal of Thermophysics and Heat Transfer*, Vol. 20, No. 4, Oct.–Dec. 2006, pp. 672–679.

[22] Goulard, R., "On Catalytic Recombination Rates in Hypersonic Stagnation Heat Transfer," *Jet Propulsion*, Vol. 28, No. 11, Nov. 1958, pp. 737–745.

[23] Winkler, E. L., and Sheldahl, R. E., "Influence of Calorimeter Surface Treatment on Heat-Transfer Measurements in Arc-Heated Test Streams," *AIAA Journal*, Vol. 4, No. 4, April 1966, pp. 715–716.

[24] Tauber, M. E., and Sutton, K., "Stagnation-Point Radiative Heating Relations for Earth and Mars Entries," *Journal of Spacecraft and Rockets*, Vol. 28, No. 1, Jan.–Feb. 1991, pp. 40–42.

T. Lin
Associate Editor